Martian exospheric density using Mars Odyssey radio tracking data

E. Mazarico,[1] M. T. Zuber,[1,2] F. G. Lemoine,[2] and D. E. Smith[2]

Received 20 April 2006; revised 30 October 2006; accepted 27 November 2006; published 30 May 2007.

[1] We present measurements of the density of the Martian atmosphere at ~400 km altitude. Our analysis used radio tracking data to perform precise orbit determination on the Mars Odyssey spacecraft between March 2002 and November 2005. Recent improvements in a priori physical models make it possible to isolate the contribution of the atmospheric drag from the various forces acting on the spacecraft. For each spacecraft trajectory segment (arc) we adjusted an atmospheric drag coefficient (C_D), which scales the a priori model density. From the drag coefficient we obtained a time series of the measured density. These measurements at the Mars Odyssey orbiting altitude are close to noise level, and the various tests we conducted show the robustness of the measurements. We obtained a better agreement with the atmospheric model used during the second Martian year, when solar activity is lower. Using various simple exponential atmosphere models, we estimated the scale height near the spacecraft periapsis and found values between 25 and 50 km, in the lower range of expected values, and used exospheric temperature estimates to assess the role of EUV heating of the upper atmosphere. We did not observe one-to-one correlation between solar activity and exospheric density, but we detected a solar rotation periodicity in our measurements.

Citation: Mazarico, E., M. T. Zuber, F. G. Lemoine, and D. E. Smith (2007), Martian exospheric density using Mars Odyssey radio tracking data, *J. Geophys. Res.*, *112*, E05014, doi:10.1029/2006JE002734.

1. Introduction

[2] In this analysis we use measurements of dynamic pressure on the Mars Odyssey spacecraft to recover atmospheric drag during the mission's mapping phase. From the measured drag we determine the density of the Martian upper atmosphere at an altitude of 400 km.

[3] From an engineering perspective, drag measurements are important for spacecraft navigation and can become critical for lander entry design. In the upper atmosphere, the short- and long-term density variations due to the solar, seasonal and diurnal cycles and dust storms can be significant. In addition to operational navigation, density measurements at high altitudes can also prove valuable in terms of planetary protection. Additional density measurements at high altitudes can also help define appropriate quarantine orbits, on which to place spacecraft at the end of their mission, to prevent them from colliding with Mars on decadal timescales (Category III missions [*NASA*, 2005]). Measurements near 400 km are essential, given that the current plan for the Mars Global Surveyor quarantine is to raise its orbiting altitude to 405 km [*Mars Global Surveyor Project,*1995, section 2.2.5]. Scientifically, current atmospheric modeling efforts push general circulation models (GCMs) to include increasingly greater portions of the Martian atmosphere [*Haberle et al.*, 1999; *Justus et al.*, 2002; *Bougher et al.*, 2004; *Lewis and Barker*, 2005; *Angelats i Coll et al.*, 2005; *Bougher et al.*, 2006], which approaches the altitude of the measurements presented here. Thus from both scientific and practical standpoints the variability of the atmosphere needs to be better assessed.

[4] Radio occultations by Mars Global Surveyor (MGS) have provided several thousands density profiles in the lower atmosphere [*Hinson et al.*, 1999; *Tyler et al.*, 2001]. Data measurements that can be used as upper boundary conditions for GCMs are critical but sparse below 200 km, and almost nonexistent above. Important data has been acquired by accelerometers during the aerobraking phases of MGS and Mars Odyssey, at lower altitudes (100–170 km [*Keating et al.*, 1998; *Tolson et al.*, 2005; *Withers et al.*, 2003; *Withers*, 2006]). Measurements below 220 km are also possible with remote sensing techniques (limb scanning, air glow, electron reflectometry, stellar occultations). As noted by *Bruinsma and Lemoine* [2002], drag measurements by Mars Odyssey made at 400 km can be valuable for a better understanding of the Martian thermosphere, as a complement to existing data sets.

[5] In this work, we retrieve atmospheric densities at the orbital altitude of Mars Odyssey, using X band radio tracking data and Precision Orbit Determination (POD thereafter). This has been done extensively with Earth-orbiting satellites [e.g., *Jacchia and Slowey*, 1962] and, more recently, by *Konopliv et al.* [2006] and *Forbes et al.* [2006] for Mars. After introducing the data and methods used to estimate the density (section 2), we present the

[1]Department of Earth, Atmospheric and Planetary Sciences, Massachusetts Institute of Technology, Cambridge, Massachusetts, USA.
[2]Solar System Exploration Division, NASA Goddard Space Flight Center, Greenbelt, Maryland, USA.

Copyright 2007 by the American Geophysical Union.
0148-0227/07/2006JE002734

analysis of the tracking data (section 3), the results and their significance (section 4) for Martian atmosphere structure.

2. Data and Methods

[6] The Mars Odyssey spacecraft was launched in April 2001 and performed its insertion maneuver into Mars orbit October of that year. As for the earlier Mars Global Surveyor mission, Mars Odyssey underwent a period of aerobraking [*Mase et al.*, 2005; *Smith and Bell*, 2005; *Tolson et al.*, 2005; *Withers*, 2006] to transform its initial polar, elliptical orbit to a circular mapping orbit at an altitude of $\approx$ 400 km. The spacecraft advantageously used the atmospheric drag near the periapsis ($\approx$110 km) of its initial elliptical orbit to remove energy from the orbit and progressively decrease the apoapsis. Odyssey's aerobraking phase was completed on 19 February 2002, and science operations began shortly thereafter. Here we use the available radio-tracking data set during the nominal mission (March 2002 to August 2004) and extended mission (August 2004 to November 2005), i.e., about 2 Martian years total.

2.1. Mars Odyssey Orbit

[7] Mars Odyssey has an orbit quite similar to Mars Global Surveyor: a retrograde polar orbit (i $\approx$ 93.1°) with a semimajor axis corresponding to a mean altitude near 400 km and an orbital period of just under 2 hours ($\approx$118 min). With this inclination and an appropriate phasing, the orbit is nearly Sun synchronous (fixed equator-crossing time), which allows for good solar energy input (the eclipse duration never exceeds 25% of the orbit). Although Odyssey's orbit is nearly circular, its eccentricity oscillates between 0 and 0.013 (average of $\approx$0.008) with a period of $\approx$74 days [*Pace et al.*, 2000]. The altitude of the spacecraft varies between 390 and 450 km.

[8] The Mars Odyssey orbit is "frozen" [*Cutting et al.*, 1978], such that the periapsis is always located above the South Polar region, near 85°S. However, contrary to MGS, the afternoon local mean solar time (LMST) drifted, from $\approx$4 am/pm to $\approx$5 am/pm between January 2002 and October 2003 [*Mase et al.*, 2005] (Figure 1). A maneuver on 20 October 2003 stabilized the LMST at 5 am/pm and put Odyssey into its Sun-synchronous configuration. Nevertheless, due to the eccentricity of Mars' heliocentric orbit, the local true solar time (LTST) continued varying between $\approx$4pm and $\approx$6pm.

[9] Odyssey's orbit experiences more significant changes in the Sun beta angle ($\beta_\odot$) than did MGS (Figure 1). $\beta_\odot$ is the angular separation between the Sun-Mars line and the orbit plane.

2.2. Radio Tracking Data

[10] The radio signals received (uplink) and transmitted (downlink) by the Mars Odyssey Telecommunication system have frequencies at X band (7.2 GHz uplink, 8.4 GHz downlink).

[11] In addition to a fully redundant electronics subsystem, the 1.3-m-diameter parabolic high-gain antenna (HGA) is supplemented by a medium-gain antenna (MGA) and a low-gain antenna (LGA). When the spacecraft is in safe mode, the LGA is used for reception (because of its large beam width) and the MGA for transmission. (There were two instances of safe mode over the course of the primary science mission: 3 days in November 2002 and 8 days in November 2003).

[12] The HGA is mounted on a two-gimbal articulated arm, which enables it to point over a large solid angle. This permits nearly continuous tracking by the Deep Space Network (DSN, with stations in Goldstone, California; Canberra, Australia; and Madrid, Spain) while maintaining a nominal spacecraft attitude and operating the science instruments.

[13] The DSN ground stations act as very accurate and stable frequency sources which the spacecraft can use to generate the downlink radio signals. A frequency carrier can be generated onboard by an oscillator (SSO, sufficiently stable oscillator), but its quality (i.e., stability) is poor compared to the USO (ultrastable oscillator) onboard MGS and the Hydrogen-Maser clocks in the DSN facilities. The stability of the latter is of the order of 1 part in 10^{16} over a few hours. The radio signals generated with the SSO would not be appropriate for POD. The ratio of received and transmitted frequencies was chosen as a rational number (749/880), so that electronic frequency multipliers can generate the outgoing radio signal from the frequency of the incoming electromagnetic wave, enabling high-quality X band tracking of Mars Odyssey. Although the frequencies used by MGS are slightly different, the uplink/downlink ratio is the same and the telecommunication subsystem is very similar to the one described by *Tyler et al.* [1992].

[14] Two different types of measurements can be carried out to provide radio-tracking data to be used for the POD. The Doppler shift of the signal frequency is related to the relative velocity of the spacecraft in the line of sight. The high stability of the frequency source enables the measurement of line-of-sight velocity changes of the order of 10 μm/s. One-way (spacecraft to station) radio signals are not used to perform the POD because of the SSO. However, with the "turnaround" capability, two-way (station to spacecraft and back to the same station) and three-way (station to spacecraft and back to a different station) "Doppler measurements" are of good quality. Moreover, the frequency shift is averaged over 10 s to increase the signal-to-noise ratio. The traveltime of the electromagnetic waves puts a constraint on the position of the spacecraft. Because of the fact that transmitted radio signals have a wavelength much shorter than the actual range to be measured, and that only the phase of the received signal can be measured, a series of square waves of decreasing frequency is transmitted. As a result, "range measurements" are sparser than the Doppler ones. The data set of this study comprises $\approx$3,500,000 Doppler and $\approx$155,000 Range observations.

2.3. Precision Orbit Determination

2.3.1. Force and Measurement Modeling

[15] We used the software package GEODYN [*Pavlis et al.*, 2006] to process the radio-tracking data of Mars Odyssey over short trajectory segments (called "arcs"). Arc duration is determined primarily by the data coverage, but is usually about 5 days [*Lemoine*, 1992]. The spacecraft motion is integrated in a Cartesian frame from an initial state with a fixed integration step using a high-order Cowell

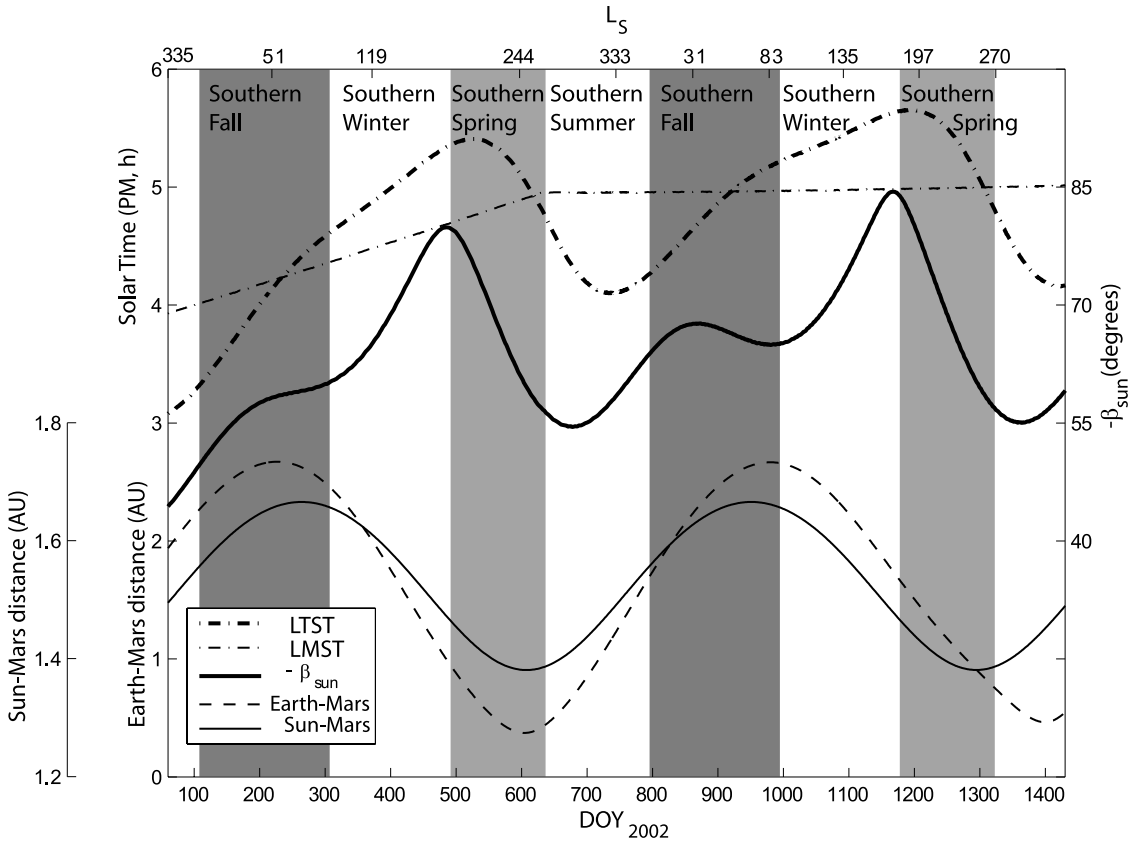

Figure 1. Near conjunction ($DOY_{2002} \approx 220$ and $DOY_{2002} \approx 980$), Mars appears close to the Sun and the quality and quantity of tracking decreases. The parameter is the elevation of the Sun with respect to the orbit plane and controls the length of the eclipses of the Sun by Mars. The local true solar time (LTST) is an important controlling parameter for the atmospheric density. The local mean solar time (LMST) is defined with respect to the fictitious Sun position if Mars' orbit was circular and represents the average LTST over a Martian year.

predictor-corrector method. Using a number of physical models for the forces acting on the spacecraft and the corrections to apply to the radio observations, the initial state and various model parameters are adjusted by a Bayesian least squares scheme until convergence is deemed satisfactory (typically a change in RMS (root-mean-square) smaller than 2% compared to the previous iteration).

[16] The physical models included in GEODYN are the following.

[17] 1. The first model is third-body gravitational perturbations, with ephemerides DE410 from JPL (Sun, planets, and Moon) and *Jacobson et al.* [1989] (Phobos and Deimos). DE410 is a successor model to DE403 [*Standish et al.*, 1995]. It includes recent Mars orbiter data range and delta differential one-way range (D-DOR) data, which significantly improves the Mars ephemerides modeling.

[18] 2. Gravitational acceleration due to Mars is calculated from a high-resolution spherical harmonic expansion of the gravity field. We use the GSFC solution "mgm1041c", calculated from MGS radio tracking data only [*Lemoine*, 2003].

[19] 3. Another model is relativity modeling in the force model (modification of the Mars central body term) and in the measurement model (for light time and range corrections, combined with the ephemerides).

[20] 4. Mars solid tide is explicitly modeled in the spacecraft acceleration calculation. We use the value of the tidal Love number k_2 of 0.055 [*Smith et al.*, 2001]. More recent published values are in the range 0.153–0.163 [*Yoder et al.*, 2003; *Smith et al.*, 2003]. However, because of Mars Odyssey nearly constant LMST, variations in the tidal force are expected to be small.

[21] 5. DSN ground station position corrections due to solid tides and ocean loading are included.

[22] 6. Corrections to the radio signal due to its propagation through the troposphere, dependent on local weather are used.

[23] 7. The final model is surface forces: radiation pressure (direct, reflected and planetary thermal) and atmospheric drag. The reflected and thermal radiation forces are calculated using low-order zonal spherical harmonic expansions of seasonally varying Martian albedo and emissivity maps [*Lemoine*, 1992]. The atmospheric density model used is discussed in section 4.1.

[24] For radiation and atmospheric drag forces, cross-sectional areas of the spacecraft need to be calculated. We use a macromodel to represent the spacecraft [*Marshall and Luthcke*, 1994], that consists of 10 plates with specific surface areas, orientations, and diffuse and specular reflec-

tivities (6 for the spacecraft bus, 2 for the front/back of the HGA, 2 for the front/back of the solar panel).

[25] The plates are oriented in inertial space according to the telemetered quaternions. During short telemetry data gaps, the orientation is interpolated, and a attitude model is used for longer gaps. The total surface acceleration is computed by summing the contributions of each plate from the source vector. For the atmospheric drag and direct solar radiation pressure, the source vectors are, respectively, the along-track and Sun directions. For the reflected and planetary thermal radiation pressures, the visible Martian surface is broken into multiple sources [*Lemoine*, 1992]. GEODYN does not account for self-shadowing and radiation of the modeled plates. While the instantaneous self-shadowed area can reach as much as ≈10% of the total, its phasing with respect to the orbit perihelion (and maximum velocity) leads to only a ≈3–4% misestimate over a full orbit. The POD-adjusted drag coefficients can be modified a posteriori to account for this effect.

[26] The attitude of the spacecraft is controlled using three momentum wheels. If spun appropriately, the whole spacecraft can point in the desired direction by simple conservation of angular momentum. When rotating too fast, these wheels need to be slowed down. The nonsymmetrical spacecraft configuration, with only one large solar panel and a telescopic boom for the GRS sensor, can also lead to perturbations to the spacecraft attitude that need to be corrected. Small thrusters are fired while despinning the wheels in order to keep the spacecraft fixed. The number of attitude thruster firings is generally low (about 1 per day), but as a desaturation maneuver is never perfectly decoupled (balanced), it results in a small acceleration and torque imparted to the spacecraft. Because of the low level of the atmospheric drag acceleration, it is necessary to estimate these "angular momentum desaturation" (AMD) accelerations to prevent contamination of our results.

2.3.2. Method

[27] The ≈4 years of radio-tracking data we processed were divided into 235 trajectory arcs. The arc length is the result of a trade-off between having enough observations in order to have a stable and sensitive convergence while avoiding the accumulation of force model errors. Following *Lemoine* [1992], we favored an average length of ≈5 days. The exact start and stop times were chosen based on AMD timings and data coverage, and the actual arcs are 3 to 7 days long. Inasmuch as possible, we did not include extended periods where AMD accelerations had to be estimated without tracking data.

[28] Among the various parameters adjusted by GEODYN, the drag coefficient (C_D) is the most critical in this study. It is an unconstrained scale factor of the atmospheric drag force adjusted to best fit the observations, and our density measurements depend directly on it (section 2.4). Short arcs (one station pass, i.e., a few hours) and arcs with large data gaps lead to poor estimates and low signal-to-noise ratio. To stabilize the recovered C_D values, we chose to nominally adjust it only once per arc, even though it entails poor temporal resolution of our measurements. Indeed, if adjusted too frequently, nonatmospheric perturbations are likely to perturb the adjustment of C_D, which would result in erroneous results. In other (gravity-oriented) studies, C_D is usually evaluated more often, sometimes once per orbit, but in such a case it is often viewed as a way to account for mismodeled accelerations and not necessarily atmospheric drag. As shown later, we obtain robust results and rather little contamination from other perturbations. Indeed, although the level of atmospheric drag is usually much smaller than both the direct solar and albedo radiation pressures, it is only acting along track and is of comparable magnitude with the along-track components of the other nonconservative forces (the albedo radiation is mostly radial, and the direct solar radiation is typically radial and cross track). This makes its estimation by POD possible. As presented in sections 3 and 4, we obtain a consistent time series of drag coefficients and densities, although we are probably close to noise level.

2.3.3. Density Measurements From Mars Odyssey POD

[29] The atmospheric drag acceleration implemented in GEODYN is

$$a_{drag} = \frac{1}{2}\frac{\rho C_D V^2}{m}\sum_i A_i \vec{n}_i \cdot \vec{n}_V$$

where V is the spacecraft velocity, n_V the along-track vector, A_i and n_i the surface area and normal vector of the macromodel plates facing n_V (i.e., whose angle with n_V is less than 90°) and m the mass of the spacecraft. The lateral wind and aerodynamic lift are not taken into account. The C_D factor in the equation above, commonly referred to as the "drag coefficient", is the parameter adjusted by GEODYN. It does not only represent the aerodynamic drag coefficient of the spacecraft, but is also used to scale the model atmospheric density to achieve best fit of the tracking observations:

$$\rho_{measured} = \frac{C_D}{C_C^{real}}\rho_{Stewart}$$

where C_D^{real} is the spacecraft aerodynamic drag coefficient. Given the hypersonic free molecular flow regime of Mars Odyssey, C_D^{real} is close to 2.1 (calculated computationally by *Takashima and Wilmoth* [2002] with 2.9% uncertainty; also comparable to the value for MGS of 2.13 from *Wilmoth et al.* [1999]).

[30] Thus the drag coefficients obtained in section 3.2 are not a direct scale factor of the model density: the measured density is the model density when C_D is equal to C_D^{real}, not 1. A change in C_D does not necessarily translate into a density variation.

3. Analysis of the Tracking Data

3.1. Convergence of Orbital Arcs

[31] Within an orbital arc, a large number of orbits are poorly or not tracked, and regular desaturation maneuvers need to be evaluated. With arcs several days in length, the mean trajectory of the spacecraft can be well constrained. The initial state of the spacecraft was determined with formal relative standard deviations near 10^{-7}, which correspond respectively for position and velocity to better than 1m and 1mm/s, except for a small number of arcs in 2004. These formal uncertainties are commensurate with the a priori data weights used, which are based on the quality of

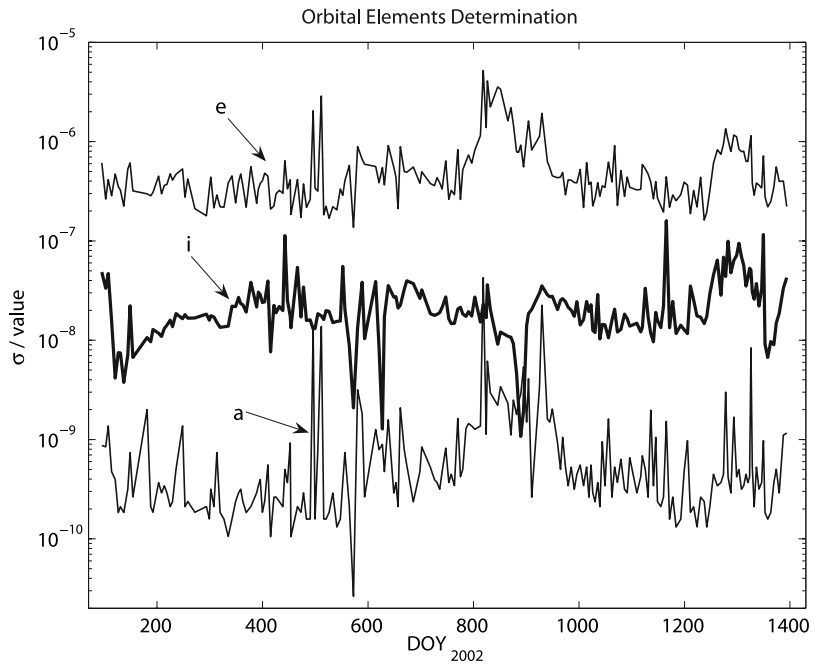

Figure 2. The relative standard deviation (σ/value) of several orbital elements of the spacecraft state at the initial time step of each arc: the semimajor axis (*a*), eccentricity (*e*) and inclination (*i*).

the tracking (we chose 1 m and 1 mm/s for the Range and Doppler measurements respectively).

[32] In addition to reducing the coverage (when viewed edge-on, the spacecraft is behind Mars half of the time), the observation geometry can worsen the quality of the Doppler measurements (when viewed face-on, the velocity vector has no line-of-sight component). Figure 2 presents the quality of the arc initial state determination (relative standard deviation) in terms of the major osculating orbital elements. The determinations are generally better than 1 part per million for the eccentricity and orders of magnitude less for the semimajor axis. We can also observe the negative correlation between the determination of the inclination *i* and that of *a* and *e* (respectively, semimajor axis and eccentricity): an edge-on geometry of the orbit when viewed from the Earth is more favorable for the estimation of *a* and *e*, whereas *i* is better constrained when the spacecraft trajectory is seen face-on.

[33] The RMS of the Doppler and range residuals (differences between actual observations and model predictions after convergence of the arc) are of the order of 0.3 mm/s and 3 m, respectively (Figure 3). A few arcs show larger values, but that does not imply they are poorly constrained (Figure 2). During periods of solar conjunction, the number of range measurements decreases significantly, dropping to zero near conjunction. The quality of the data is also affected and the POD is noisier, due in part to mismodeled signal distortion by solar plasma (near $DOY_{2002} \approx 220$ and $DOY_{2002} \approx 980$).

3.2. Drag Coefficient

[34] Figure 4 shows the time series of the C_D and C_R coefficients estimated for each arc. For each arc, the C_D and C_R are unconstrained and adjusted, with other parameters, to achieve best fit to the radio tracking observations. A small number of drag coefficients adjust to negative or anomalously high values. Those were discarded as nonphysical, and are mostly due to poor adjustment by GEODYN because of large data gaps. The adjustments are totally independent from arc to arc, but clear trends are visible in both curves.

[35] There is a high temporal correlation in our C_D estimates: a trend is clearly visible in arc-to-arc values. The few data points that fall far from that trend were removed at this point. We think that the consistency in the independently adjusted C_D stems from a real signal, indicative of atmospheric changes. Indeed, formal C_D standard deviations are usually around 1% of the adjusted value, but increase to about 10% near $DOY_{2002} \approx 950$. The real uncertainties in the retrieved densities are difficult to assess, but given the robustness of the drag coefficient adjustments in both long and short arcs (section 3.2.4), we believe that uncertainties about 5 times the formal ones would be reasonable.

3.2.1. C_R Trend

[36] An unconstrained scaling factor for the solar radiation pressure acceleration (C_R) was also adjusted by GEODYN. Its value is expected to be near unity because the solar flux is a constant once the eccentricity of Mars orbit has been taken into consideration. However, some mismodeled or unmodeled nonconservative forces (approximate surface properties, no interplate reradiation, no spacecraft thermal emission) are expected to be absorbed in the C_R estimate.

[37] The adjusted C_R coefficients for Mars Odyssey show remarkable temporal consistency (Figure 4), with values close to unity, but follow a trend strongly correlated to the $\beta_\odot$ angle (section 2.1 and Figure 1). We have no definitive explanation for this trend, and as mentioned above, given our imperfect modeling of the nonconservative forces we do

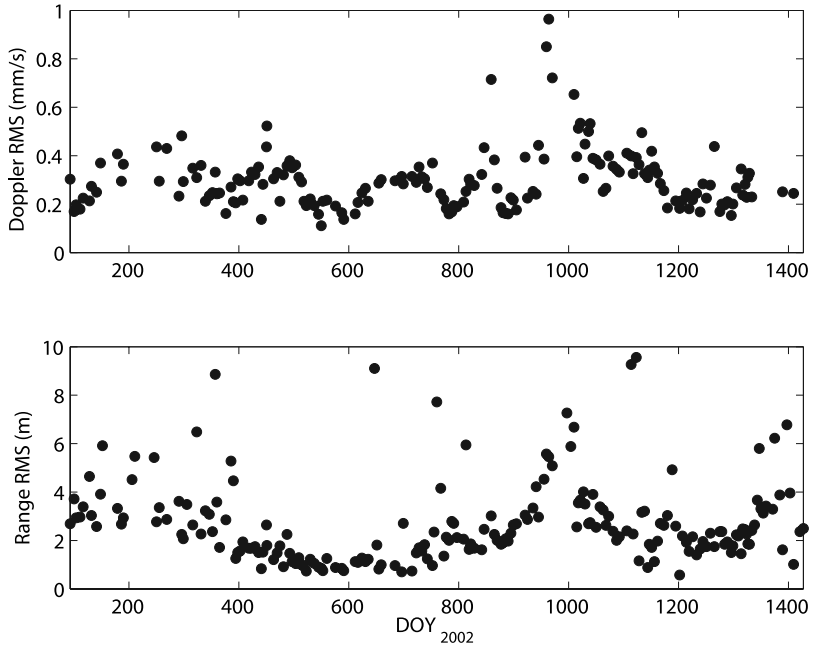

Figure 3. RMS of the observation residuals (i.e., the difference between data and the best fit model trajectory reconstructions). Units are (top) mm/s for Doppler residuals and (bottom) meters for range residuals. The range RMS is correlated with Earth-Mars distance, but the Doppler RMS is less sensitive to the geometry, except near solar conjunction ($DOY_{2002} \approx 220$ and $DOY_{2002} \approx 980$).

not expect to obtain a perfectly flat C_R time series. While the dependence of our recovered C_R on a parameter linked to the orbit geometry is troublesome because of its potential implications on our C_D results, we present below the results of robustness tests conducted to establish the independence of C_D and C_R and the robustness of the obtained C_D coefficients.

3.2.2. $C_R = 1$ test

[38] We did reprocess the whole data set while fixing the C_R coefficient to 1. Given that the solar radiation acceleration is more than one order of magnitude larger than the atmospheric drag, this constraint imposes a relatively large acceleration to be adjusted in different ways by GEODYN (among others, the initial state and the C_D coefficient).

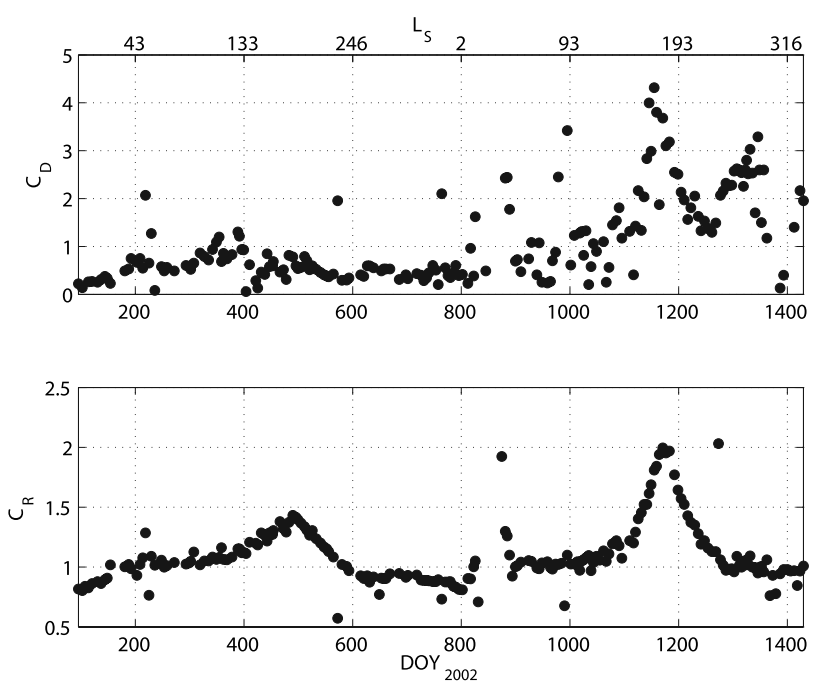

Figure 4. Time series of the drag and radiation coefficients adjusted by GEODYN.

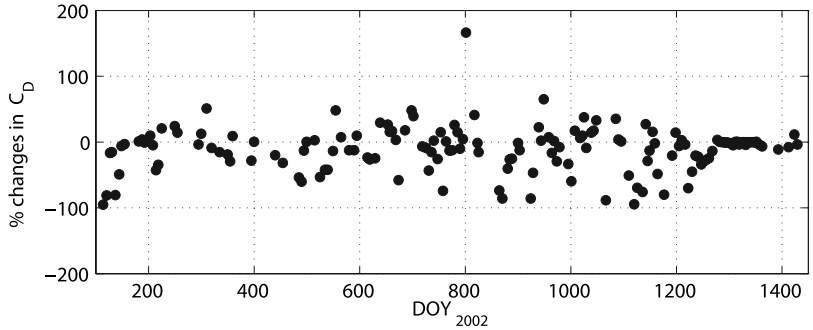

Figure 5. Changes, expressed in percent, in the drag coefficient C_D resulting from constraining the radiation coefficient C_R to unity.

[39] The changes induced in C_D (in percent) are presented in Figure 5. These can be large, and show that large forced changes in C_R impact the recovered C_D coefficient. However, it is important to note that in the time series of the magnitude of these changes, the earlier $C_R/\beta_\odot$ trend has disappeared. The angle between the solar radiation and atmospheric drag accelerations is, on average, $\beta_\odot$. However, both the large variations in $\beta_\odot$ and in the magnitude of the acceleration (scaled by C_R-1, almost always positive, meaning that the forcing is always in the same direction relative to the orbit and the drag) are not visible in the C_D changes (Figure 5), which cluster nearly randomly around a small mean (−4%). In addition, we note that the Doppler RMS generally increases by more than 20%, and is sometimes doubled. Thus the mismodeled force responsible for the C_R trend cannot be accounted by a change in C_D when forced to, but only leads to poorer convergence when we fix C_R to 1.

[40] This leads us to think that the unexplained and anomalous acceleration that contaminates C_R has no atmospheric origin; and that the large changes observed in C_D are the result of forcing GEODYN to account for that acceleration solely in the form of atmospheric drag. These changes, about 30% on average, may represent upper bounds on the uncertainties in C_D due to physical mismodeling. In addition, the formal covariance between C_D and C_R established by GEODYN within each arc is small, less than 0.1, compared to values close to 1.0 when a correlation is expected (e.g., Cartesian components of the initial velocity or position of the spacecraft).

[41] Not adjusting the radiation coefficient is very unrealistic, because of modeling uncertainties, and it is usually not done in practice. Thus, in order not to overconstrain the solution and to be able to distinguish between bad C_D estimates and artificial contamination due to fixed C_R, the following results are for unconstrained C_R coefficients.

3.2.3. Comparison With C_D Obtained From Another Set of Arcs

[42] In section 2.3, we mentioned that the arcs were created based on data coverage and thruster firing timings. Because of the very low level of drag acceleration that we need to discriminate, we evaluated the influence of our choice of arcs on the obtained values. The objective is to show that the frequent data gaps and the regular AMD estimations do not significantly influence the recovery of the C_D and C_R.

[43] The arc lengths are different so the number of AMDs and gaps are different. The new arcs are not as "good" as our primary choice, and sometimes include relatively long periods at the beginning of the arcs without data. The new C_D and C_R values are shown in Figure 6. The trend is unchanged, and the changes are of the same order of what could be expected from arc-to-arc atmospheric variability alone (about 50%; Figure 6, open symbols). In addition, the adjusted C_D values are closer when the arc overlap is more significant. The same is observed for the radiation coefficient C_R. We note that C_R is not as sensitive to the change in arc length as C_D, mainly because the solar radiation is a stronger acceleration, easier for GEODYN to adjust as it affects the overall convergence.

[44] Thus the contamination of our results due to arc length, epoch time and AMD acceleration estimation seems to be limited to an average ∼20% in C_D. This indicates that the results are largely independent of the manner in which we chose the initial orbital arcs and provides additional support for the conclusion that the retrieved C_D values are representative of actual changes in atmospheric density.

3.2.4. Comparison With Daily C_D Coefficients

[45] Our general ability to properly estimate the atmospheric density scale factor with GEODYN was assessed by increasing the temporal resolution and evaluating the stability of the recovered drag coefficients. We estimated C_D once per day instead of once per arc (i.e., 3–7 days). Because of data gaps inside the arcs, a nonnegligible number of 1-day intervals were insufficiently constrained and resulted in anomalous coefficients (≈15% of the total number) that we discarded. Indeed, with large data gaps in a 24-hour period, the drag acceleration adjustment is less constrained and is more subject to contamination by mismodeled forces. Nevertheless, the majority of coefficients fell within the range of C_D adjusted previously (Figure 7), and thus may represent actual atmospheric variability.

[46] Here arc convergence is not affected, and the radiation coefficients unchanged. We tried reducing the adjustment intervals to values comparable to the orbital period (≈2 hours), but that resulted in nearly random coefficients.

[47] We used these more frequent drag coefficient estimates in order to estimate the intrinsic density variability (which can also be seen as an uncertainty) of our ≈5-day-

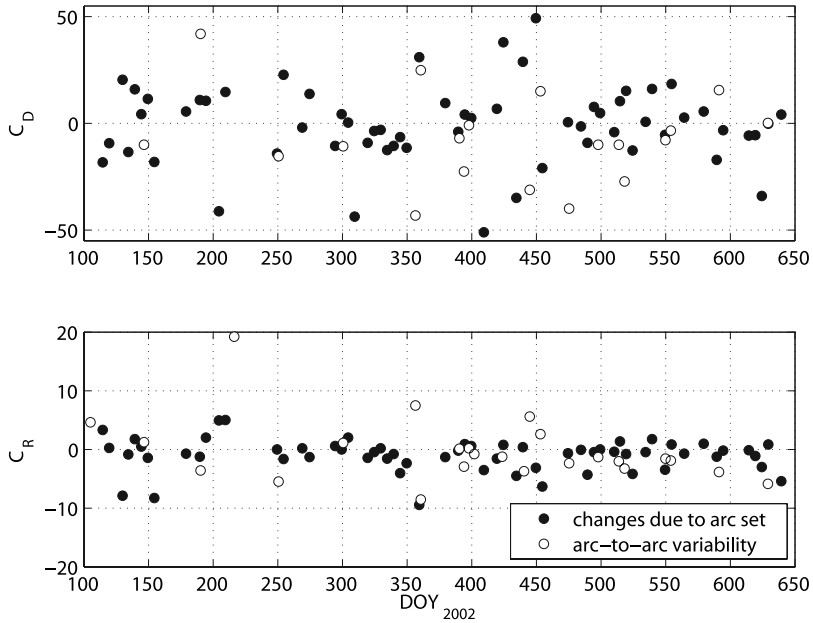

Figure 6. Changes in C_D and C_R due to a change of arc set (solid circles). For comparison, the arc-to-arc variability (within the primary set of arcs and of very close arcs only) is also plotted.

averaged recovery. For each arc, we estimate the standard deviation of the daily estimates with respect to the C_D obtained over the entire arc (Figure 7, bottom). The observed variability is not due to computational issues. Indeed, in general, the variability within the long 5-day arcs is about 10%, although values below 50% are common (but do not seem correlated to either geometry or seasons), well above the level of uncertainties in the C_D values.

3.2.5. Periodicity Within the C_D Time Series

[48] We also checked for periodicities in the C_D time series, in order to detect the signature of the solar rotation in our measurements. That signature, in density, has been observed both on the Earth (with CHAMP) and on Mars (with MGS) by *Forbes et al.* [2006].

[49] We expect to see that signature in the C_Ds as well, because they are adjusted from the Stewart model, which

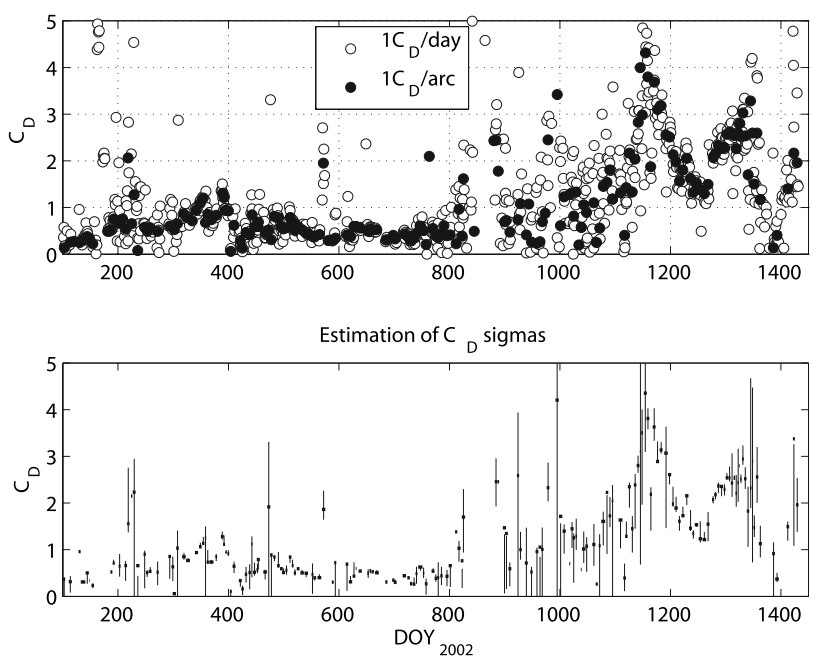

Figure 7. (top) Daily estimates of the drag coefficient (open circles), showing a significant scatter around the arc_long values (solid circles). (bottom) Scattered daily values used to evaluate the C_D variability versus time. The scatter provides a measure of the sensitivity of atmospheric density recovery to the length of the averaging window (arc).

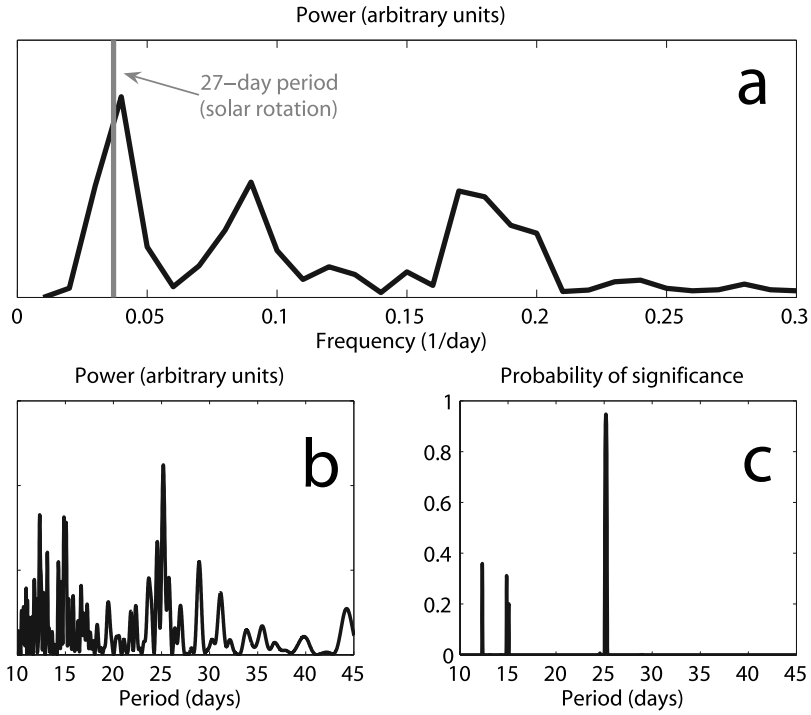

Figure 8. Frequency analysis of the C_D residuals: power spectrum (a) using FFT, after interpolation to obtain an evenly-spaced time series and (b) using Lomb's method for unevenly spaced data, power spectrum and (c) probability of peak significance.

uses an 81-day averaging of actual solar flux (therefore removing the solar rotation periodicity from the model estimation; see section 4.1). As noted by *Withers and Mendillo* [2005], due to the difference in the planets' orbital periods, the observed solar rotation seen from Mars should have a 26 day periodicity rather than 27 days observed on Earth.

[50] We performed this analysis on drag coefficient residuals (actual $C_D - C_D$ smoothed over 26 days). We used the daily estimates rather than the arc-long values whose 5–7 day sampling is not appropriate to detect a ≈26 day period.

[51] The uneven sampling of the time series (which depends on the arcs themselves, i.e., data coverage) renders the use of an FFT problematic. By interpolating the data at a frequency of a fraction of a day, we could obtain a power spectrum (Figure 8a), but it is hard to say whether it was contaminated by interpolation artifacts. Nevertheless, the most significant frequency seems to be ≈27 days, close to the solar rotation period.

[52] To answer this issue of uneven sampling, we used Lomb's method [*Lomb*, 1976]. We obtain a single significant frequency of ≈25.2 days (at 98.5% confidence) (Figures 8b and 8c). While this period is a lower than the expected solar rotation period, such a strong frequency in our data suggests we detect the effects of the solar input on Mars atmosphere.

[53] This analysis demonstrates that our measure of the atmospheric drag obtained from the Mars Odyssey represents actual changes in the atmospheric density at the spacecraft altitude. In the next section, we discuss these results regarding the atmospheric structure near 400 km. The atmospheric signal in the processed MGS tracking data [*Forbes et al.*, 2006] was very faint. Given the altitude difference (≈20 km), the densities sampled by Mars Odyssey are 2–3 times smaller, and the Mars Odyssey atmospheric signal is closer to the noise level. Thus the reader should keep in mind that even after much care in the processing of the tracking data with the state-of-the-art GEODYN program, not all the features we could expect can be observed in the obtained time series.

4. Atmospheric Results

4.1. Exosphere, Stewart Model

[54] With a mean altitude near 400 km, the spacecraft is in the heterosphere, where diffusion is the main transport process: air molecules do not interact much by collisions, and follow ballistic, orbital or escape trajectories. The distribution with altitude of each atmospheric species follows its specific photochemistry. This is in contrast with the homosphere below, where all the species follow the same transport laws (collision), and the mixing ratios can be considered constant. The boundary between these two layers varies between 115- and 130-km altitude with the seasons and the solar activity [*Stewart*, 1987; *Bougher et al.*, 2000]. In the heterosphere, the temperature increases with altitude asymptotically up to a maximum value (the exospheric temperature) determined by the solar activity. The upper part of the heterosphere (above ≈250 km for Mars) is called the exosphere, because light particles (mainly atomic hydrogen) can escape [*Chassefière and LeBlanc*, 2004]. The heating of the exosphere by solar radiation is

largely due to the EUV (extreme UV) radiation. However, the radiation at 10.7 cm wavelength, characterized by the $F_{10.7}$ index, has historically been used in atmospheric modeling. Indeed, both radiations originate from the same region of the Sun atmosphere (and show a good correlation) and the 10.7 cm radiation can be readily measured on the ground (at the Penticton site in Canada).

[55] The numerical value used for $F_{10.7}$ is actually an average over 3 solar rotations of the daily values. The main reason for doing this is that the $F_{10.7}$ index is measured on Earth, and depending on the Earth-Sun-Mars geometry the instantaneous value may not be relevant to the radiation environment on Mars.

[56] The heterosphere itself can be subdivided into a thermosphere and an exosphere. In the exosphere where the Mars Odyssey spacecraft orbits during its science mission, molecules can escape the atmosphere (atomic H mainly through Jeans escape [*Chassefière and LeBlanc*, 2004]), and light gases become significant. From the model presented below, in terms of number density, the major components near 400 km and for average conditions are He, H_2, H and O [*Stewart*, 1987; *Krasnopolsky*, 2002]. In terms of mass density, which is more relevant to the current study, the main contributors are O, He, N_2 and CO.

[57] The atmospheric model used in GEODYN during POD is based on Stewart's thermospheric model [*Stewart*, 1987], with modifications [*Lemoine et al.*, 2001]. The turbopause altitude is calculated using an empirical formula; the reference 6.1 mbar altitude is corrected for time-dependent effects (seasonal global pressure variation, seasonal dust opacity variations of an average year); the solar activity ($F_{10.7}$) sets the exospheric temperature. L_S is the areocentric longitude of the Sun, used to refer to the Martian seasons; it varies between 0° and 360°. By convention, the first Mars year (MY) began on 11 April 1955, so the Mars Odyssey data used here is from late MY-25 to late MY-27.

[58] The model atmospheric density can vary by nearly two orders of magnitude due to solar activity. The impact of the seasonal cycle is not as significant, and may be due largely to the varying heliocentric distance modulating the solar input in the atmosphere. With varying solar activity (heating from EUV photons), the temperature of the exosphere varies, and in turn the relative contribution of various atmospheric species is modified.

[59] The Stewart model is based on scarce data near solar minimum; the main constraints on the atmospheric structure are the atmospheric composition profiles acquired by the mass spectrometers on the two Viking landers [*Nier and McElroy*, 1977]. Mars Odyssey orbits at local solar times near 3–5 am/pm, where the atmospheric structure can differ from the global average. However, most of the calculated partial densities are global mean values, although the atomic oxygen density does have a solar time dependence. The exospheric temperature dependence on solar activity ($F_{10.7}$) is extrapolated from measurements at low solar activity ($F_{10.7} < 60$ at Mars) using a linear regression.

[60] Using a simple random error approach, we quantified the magnitude of the uncertainties in the model density. We first calculated its sensitivity to small variations in relevant (controlling) parameters for a range of L_S and $F_{10.7}$ indices. Using estimates of the uncertainties or intrinsic variations of these parameters (5% uncertainty in $F_{10.7}$, 10% for most of the other parameters), we obtained an overall density uncertainty (Figure 9). The solar activity, through $F_{10.7}$ and the exospheric temperature, is the main contributor [*Stewart*, 1987]. However, in terms of seasonal and solar effects, the Stewart model exhibits large differences when compared to more recent models, such as Mars-GRAM (section 4.3).

4.2. Effective Atmospheric Sampling

[61] As explained in section 2.3.2, the temporal resolution of our measurements is of the order of several days, which prevents the precise study of short-lived phenomena. During one arc, the spacecraft orbits the planet several tens of times, so that no longitudinal localization of the measured density is possible. In addition, with the small amplitude of altitude variations (low eccentricity), the whole orbit contributes to the measured density. This globally averaged measurement is weighted toward the southern latitudes, due to Mars Odyssey's periapsis being located at ≈85°S. The flattening of the planet tends to extend the part of the orbit with largest atmosphere densities and drag force. The actual atmospheric drag is the density weighted by the square of the velocity of the spacecraft, which amplifies the simple altitude effect. We can calculate the effective density sampled by the spacecraft. However, we chose to present a density time series referenced to an altitude of 400 km over the South pole, for two reasons. First, over the course of the mapping mission, Mars Odyssey orbital parameters experience slight perturbations, undermining the direct interpretation of a time series of the effective sampled density. Second, that time series is actually very similar to a time series of the density above the South pole, except for an offset due to the altitude difference.

[62] It is also important to recall that the local solar time of the spacecraft is almost fixed and that we cannot separate the thermal tide effect from the mean density signal. The results presented here are indicative of the density in the spacecraft environment and not of an average density over the whole southern hemisphere.

[63] The measurements are thus more suitable for the general monitoring of the atmospheric density at the spacecraft orbital altitude, and would not be appropriate for studies of the dynamics of the exosphere or small-scale structures.

4.3. Comparison of the Results to the Model

[64] As shown on Figure 9, the measured densities are usually smaller than the model predictions. During the first Mars year of measurements (i.e., $DOY_{2002} < 800$) the discrepancy is larger than what could be expected from model uncertainties calculated previously, arguing for erroneous modeling in that time period. During the second Mars year, the agreement is more satisfying, with differences generally of the order of ≈ 2 compared to up to an order of magnitude earlier.

[65] In section 4.1, we noted that the solar activity effects on density in the Stewart model is based on a fit from measurements near solar minimum. With a solar minimum in late 2006, the better agreement between model and measurements during the second half of the time series might not be surprising. The definite discrepancy observed in 2002–2003 might be due to mismodeling at higher solar

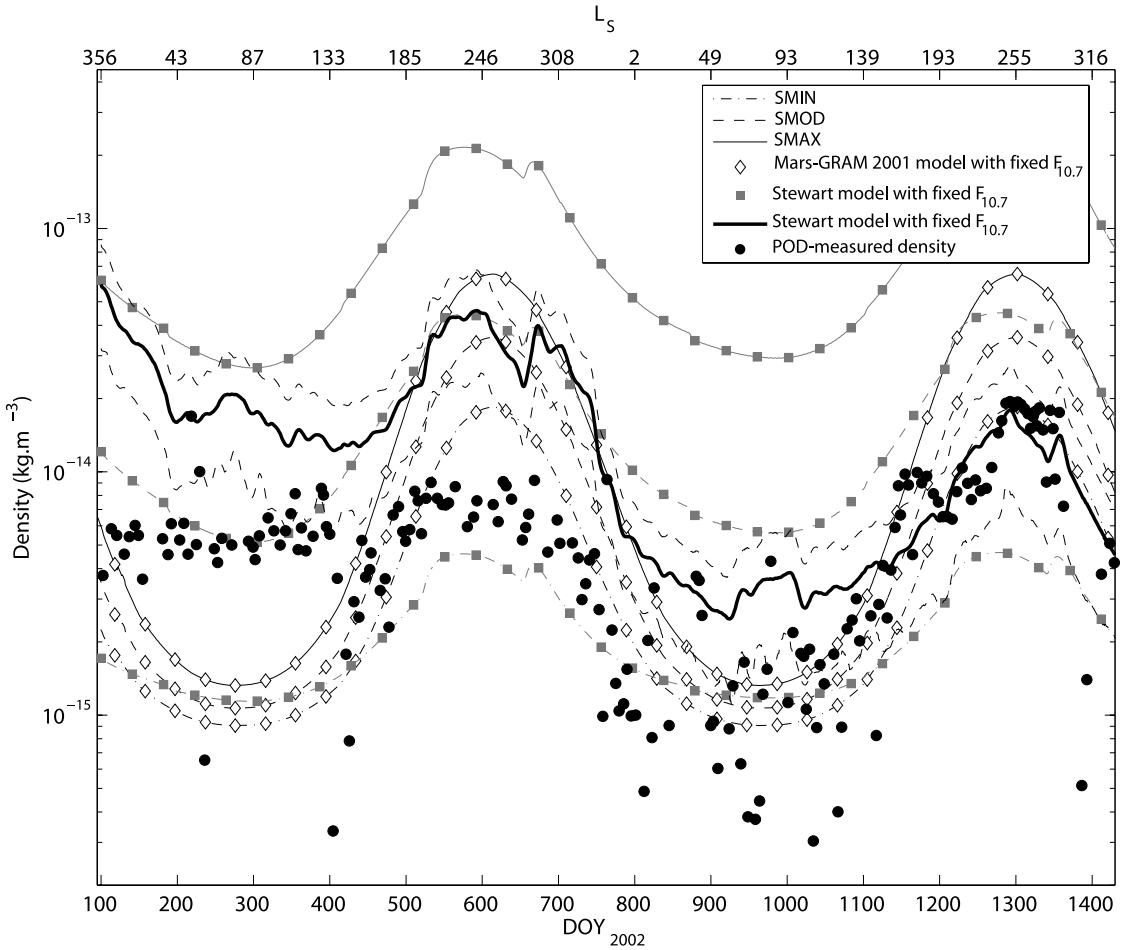

Figure 9. Time series of the measured atmospheric density. Each solid circle corresponds to an arc-long estimate. The model density and its calculated uncertainty (section 4.1) are shown (dashed line). In the background we show densities predicted by two models with $F_{10.7}$ held constant at values representative of low (dot-dashed line), moderate (dashed line) and high solar activity (solid line): the *Stewart* [1987] model we used as an a priori (squares) and Mars-GRAM 2001 (diamonds).

activity. On Figure 9, we also plotted the density predictions by the *Stewart* [1987] model and the more recent Mars-GRAM 2001 (Mars-GRAM models have not been integrated into GEODYN due to ITAR regulations on Mars-GRAM which would seriously restrict the distribution of GEODYN, in particular to its numerous foreign users) [*Justus and Johnson*, 2001], with $F_{10.7}$ held constant at values representative of low, moderate and high solar activity. The two models display very different behavior with respect to solar and seasonal forcing. The density from the Stewart model is enhanced by a factor of ≈60 between solar minimum and solar maximum, whereas Mars-GRAM 2001 only shows a maximum fourfold increase. On the other hand, for a fixed $F_{10.7}$, the seasonal density variations are much larger in the Mars-GRAM model. Our density measurements are in general bounded by the predictions of both models.

[66] The importance of solar input on the atmospheric density is illustrated in Figure 10, which plots the density versus L_S (season). Between $DOY_{2002} \approx 100$ and $DOY_{2002} \approx 800$ (MY-26), the $F_{10.7}$ index at Earth is moderate to high, with values between 100 and 200; it then slowly decreases to ≈80 near $DOY_{2002} \approx 1400$ (end of MY-27). The density differences between the two Martian years are more significant during the 0–180° period, where the contrast in $F_{10.7}$ from year to year is larger. In the second part, 180–360°, where solar activity levels in both Mars years are comparable, the measured densities show less variation.

[67] During MY-27, Figures 9 and 10 also show that the measured seasonal density contrast is more than one order of magnitude. This is larger than the predictions from Stewart (for all $F_{10.7}$), but close to Mars-GRAM 2001 with moderate or low solar activity.

[68] Even though our measurements do not agree completely with either model, it is interesting to see that our results concur with some aspects of each. Also, we find our results in better general agreement with Mars-GRAM 2001, more recent and based on more data (especially concerning light neutral gases which are major contributors in that part of the exosphere).

[69] Because no global dust storm occurred during the timeframe of our measurements (the last having taken place

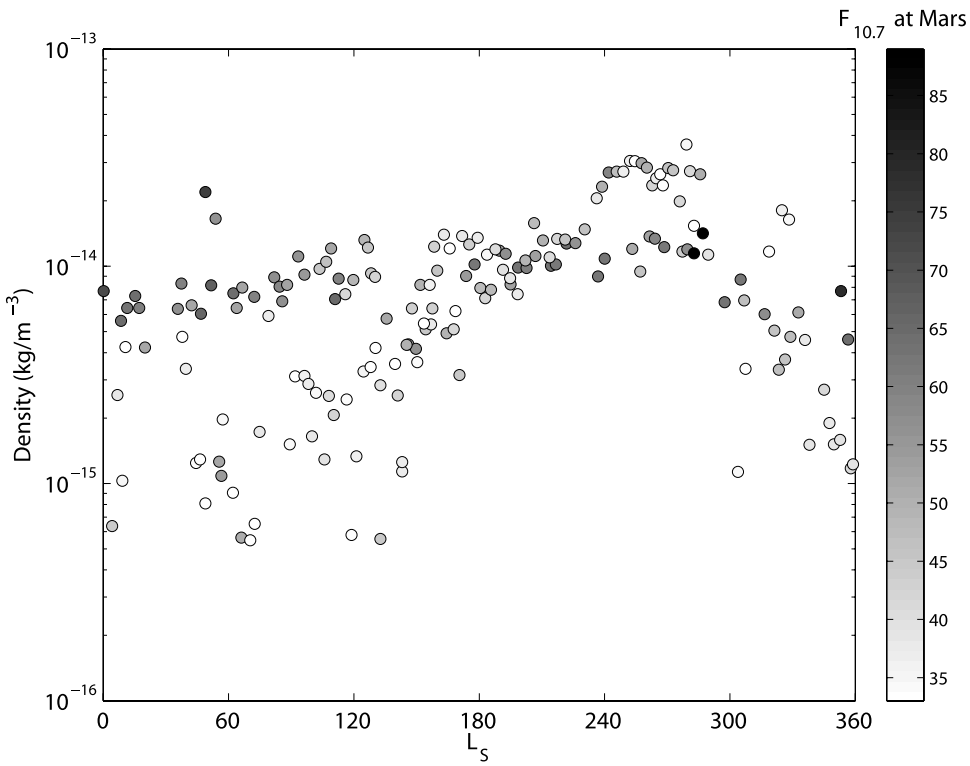

Figure 10. Measured density plotted versus the season (L_S). Darker shading indicates higher values of the solar index $F_{10.7}$ at Mars.

in 2001, mid-MY-25), we could not conclude on correlation between dust opacity and exospheric density levels.

4.4. Scale Height Estimates

[70] The single coefficient adjusted by GEODYN to recover the density is not sufficient to obtain estimates of the atmospheric scale height at the spacecraft altitude. It adjusts an "average density", resulting from the integrated atmospheric drag over a period of several days. The atmospheric structure assumed by the Stewart model enters the result, but does not put any constraint on the real atmosphere: the adjusted C_D has the value that best fits the observations, i.e., that minimizes the misrepresentation of the atmosphere by the model.

[71] Nevertheless, analytical work [*King-Hele*, 1987] provides a way to estimate the scale height near the orbit periapsis, if we assume the atmosphere can be locally represented as a simple exponential atmosphere (a reasonable assumption for our study). King-Hele showed that the density at a half-scale height above the periapsis altitude is largely insensitive to misestimates in the scale height H. An error of 25% produces a 1% density change at that altitude, and a 50% error a 3% change. Therefore an estimate of the scale height can be obtained from the altitude of intersection of adjusted simple exponential profiles. Martian exospheric models predict a large range of scale heights near 400 km, between 30 and 90 km depending on the time of year [*Culp and Stewart*, 1984; *Stewart*, 1987; *Justus et al.*, 2002].

[72] We reprocessed the whole Mars Odyssey data set using simple exponential density models characterized by respective scale heights 30, 50, 70, and 90 km. The arcs using these various models are equivalent in terms of convergence and residual RMS, so that we average the scale heights obtained from the intersection of model pairs.

[73] We obtain scale heights in the lower range of what is predicted by the models, mostly between 25 and 45 km (Figure 11). This is significantly lower than the scale heights inferred from the Stewart model, i.e., between 50 and 60 km. A smaller scale height is consistent with the generally lower density levels observed in the early part of our data span. However, in the second Mars year where the model and the measurements are roughly consistent, the scale height exhibits the same discrepancy, which is surprising and hard to explain.

4.5. Solar Rotation Effects

[74] In section 3.2.5, we presented the detection of the solar rotation in the drag coefficient time series. The density time series also displays a ≈26 day periodicity. Using Lomb's method, two periods, ≈24 and ≈25.7 days, present a peak in the power spectrum, significant at >99% and >86% probability respectively. Arc-to-arc variability and the superposition of longer (seasonal) periods to the solar rotation could explain the observed splitting in frequency.

4.6. Solar Activity Effects

[75] Unlike *Forbes et al.* [2006], we do not observe a very high correlation between the density residuals and the $F_{10.7}$ residuals (here, residuals are defined as the instantaneous value minus a smoothed value). When fitting a straight line to a scatterplot of density residuals versus

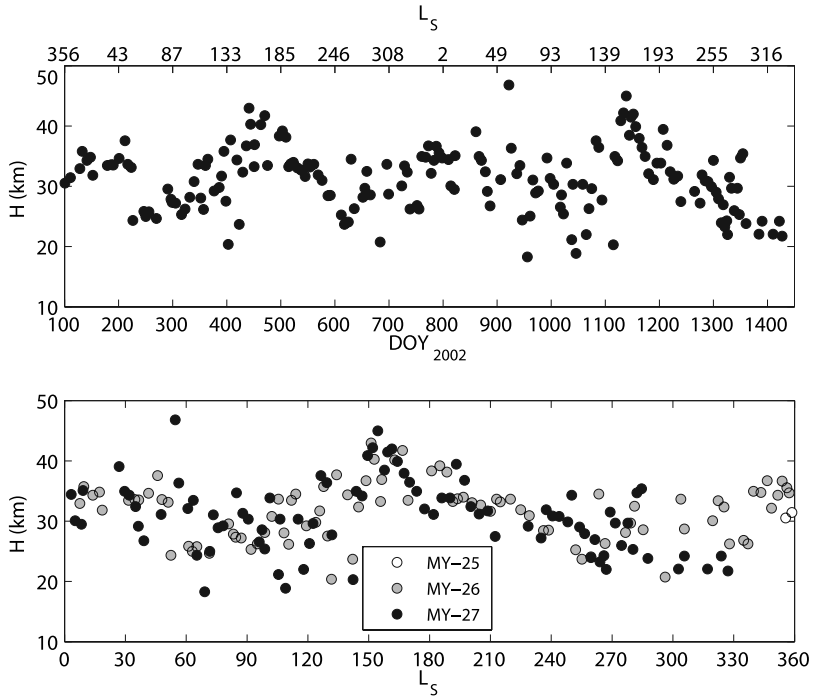

Figure 11. (top) Estimated scale height at the spacecraft periapsis, which ranges from ≈20 km to ≈50 km. (bottom) Estimated scale height plotted against L_S, which shows that it appears that the scale height is quite repeatable from year to year.

$F_{10.7}$ residuals, we obtain a shallower slope than *Bruinsma et al.* [2006], with larger misfits. As a result, a linear regression using measured $F_{10.7}$ values only yields a rather weak correlation with the $F_{10.7}$ time series (≈0.6). The lower signal-to-noise ratio compared to MGS [*Forbes et al.*, 2006] might explain why, for the same change in $F_{10.7}$ from average condition, we do not observe as strong an increase in density. Nevertheless, we note that the residuals calculated using a smoothing period of 26 days (the effective solar rotation period at Mars) result in the best fit.

[76] In section 3.2.5, we presented the detection of the solar rotation in the drag coefficient. In addition to the atmospheric structure, the recovery of the scale height near 400 km can provide constraints on the heating and cooling processes of the exosphere. We can obtain estimates of the exospheric temperature, T_{exo}, from the measured scale height H_{geodyn}, the modeled mean molecular weight (M_w) and known parameters (gravitational acceleration g, Boltzman constant k):

$$T_{exo} = \frac{M_w g H_{Geodyn}}{k}$$

The obtained exospheric temperatures (100–200 K) are low compared to *Stewart* [1987] (200–300 K), because of the lower measured scale heights. These temperatures imply that a very efficient cooling process, such as the CO_2 cooling [*Keating and Bougher*, 1992; *Bougher et al.*, 1999, 2000; *Forbes et al.*, 2006], is counterbalancing the EUV heating. Moreover, we note that even though the exospheric temperatures predicted are usually in the 200–300 K range, the measurements on which the Stewart model is based are mostly inferences from plasma scale heights. Only two direct measurements from the Viking missions (both at very low solar activity) were used, which gave temperatures between 160 and 180 K and between 110 and 130 K respectively [*Nier and McElroy*, 1977].

[77] The exospheric temperature time series has a general negative trend consistent with decreasing solar activity. This is due in part to the dependence of the estimated temperatures on the Stewart model, which was used to constrain the mean molecular weight. The correlation of the exospheric temperature with the modeled molecular weight is high (≈0.71). Nevertheless, our measurements show large improvements in correlation with both the mean molecular weight and the $F_{10.7}$ index when we use instantaneous $F_{10.7}$ values. The molecular weight correlation improves by 15% to 0.82. The correlation with $F_{10.7}$ (lagged to account for the Earth-Sun-Mars geometry, both in terms of angles and distances) increases from ≈0.34, when using $F_{10.7}$ values smoothed over 3 solar rotations, to ≈0.54. This better agreement of our measurements (obtained from smoothed $F_{10.7}$) with instantaneous $F_{10.7}$ values suggests that the temperature variations obtained from our scale height measurements capture some of the effects of varying solar radiation on the upper atmosphere.

[78] An expected result is that the exosphere temperature seems to react rather slowly to solar EUV forcing. The RMS of the residuals after fitting T_{exo} versus $F_{10.7}$ with a straight line decreases significantly when both time series are smoothed: −25% when smoothing over 1 solar rotation, and an −52% when smoothing over 3 solar rotations. In addition, the dependence of T_{exo} on $F_{10.7}$ also becomes stronger: the slope of the linear fit increases by respectively

33 and 45%. The exosphere appears to be more responsive to long-period forcing.

5. Conclusion

[79] Using X band tracking of the Mars Odyssey spacecraft, we recovered regular density measurements in the Martian exosphere over a period of two Martian years. Despite the very low levels of drag acceleration encountered, we showed through various tests that the values obtained with this technique are robust. Until recently, direct measurements near 400 km altitude were not possible. The use of Radio Science enables the monitoring of the atmospheric density over long timescales and on a global scale, at very high altitudes. The limited spatial and temporal resolutions of the results limit our measurements to global or hemispherical averages. However, this presents the advantage of maintaining a constant sampling area, and thus offers measurements consistent over time that can be directly compared temporally. In our measured density time series, we observe some important features, such as a solar rotation periodicity, and the agreement with exospheric models is reasonable. However, in this atmospheric study of the Mars Odyssey radio tracking data, the correlation of retrieved density and solar index $F_{10.7}$ is not as high as the one seen on MGS by *Forbes et al.* [2006], which could be explained by the Mars Odyssey orbit being $\approx$20 km higher.

[80] **Acknowledgments.** We thank Stephen Bougher and an anonymous reviewer for helping significantly improve the manuscript. This work was funded by the Mars Critical Data Products Program. Major thanks go to Dick Simpson from Stanford University for archiving the raw radio tracking data on the NASA PDS Geosciences node. We also thank Dave Rowlands for support on the GEODYN software and Alex Konopliv for physical parameter values of the Mars Odyssey spacecraft.

References

Angelats i Coll, M., F. Forget, M. A. López-Valverde, and F. González-Galindo (2005), The first Mars thermospheric general circulation model: The Martian atmosphere from the ground to 240 km, *Geophys. Res. Lett.*, *32*, L04201, doi:10.1029/2004GL021368.

Bougher, S. W., S. Engel, R. G. Roble, and B. Foster (1999), Comparative terrestrial planet thermospheres: 2. Solar cycle variation of global structure and winds at equinox, *J. Geophys. Res.*, *104*, 16,591–16,611.

Bougher, S. W., S. Engel, R. G. Roble, and B. Foster (2000), Comparative terrestrial planet thermospheres: 3. Solar cycle variation of global structure and winds near solstices, *J. Geophys. Res.*, *105*, 17,669–17,692.

Bougher, S. W., S. Engel, D. P. Hinson, and J. R. Murphy (2004), MGS radio science electron density profiles: Interannual variability and implications for the Martian neutral atmosphere, *J. Geophys. Res.*, *109*, E03010, doi:10.1029/2003JE002154.

Bougher, S. W., J. M. Bell, J. R. Murphy, M. A. López-Valverde, and P. G. Withers (2006), Polar warming in the Mars thermosphere: Seasonal variations owing to changing insolation and dust distributions, *Geophys. Res. Lett.*, *32*, L02203, doi:10.1029/2005GL024059.

Bruinsma, S., and F. G. Lemoine (2002), A preliminary semiempirical thermosphere model of Mars: DTM-Mars, *J. Geophys. Res.*, *107*(E10), 5085, doi:10.1029/2001JE001508.

Bruinsma, S., J. M. Forbes, and F. G. Lemoine (2006), Solar flux variability and Mars' thermosphere densities derived from orbital tracking data, paper presented at Second Workshop on Mars Atmosphere Modeling and Observations, Cent. Natl. d'Etudes Spatiales, Granada, Spain.

Chassefière, E., and F. Leblanc (2004), Mars atmospheric escape and evolution: Interaction with the solar wind, *Planet. Space Sci.*, *52*, 1039–1058.

Crider, D. H., J. Espley, D. A. Brain, D. L. Mitchell, J. E. P. Connerney, and M. H. Acuña (2005), Mars Global Surveyor observations of the Halloween 2003 solar superstorm's encounter with Mars, *J. Geophys. Res.*, *110*, A09S21, doi:10.1029/2004JA010881.

Culp, R. D., and A. I. Stewart (1984), Time-dependent model of the Martian atmosphere for use in orbit lifetime and sustenance studies, *J. Astronaut. Sci.*, *32*, 329–341.

Cutting, E., J. C. Frautnick, and G. H. Born (1978), Orbit analysis for Seasat-A, *J. Astronaut. Sci.*, *26*, 315–342.

Forbes, J. M., S. Bruinsma, and F. G. Lemoine (2006), Solar rotation effects in the thermospheres of Mars and Earth, *Science*, *312*, 1366–1368.

Haberle, R. M., M. M. Joshi, J. R. Murphy, J. R. Barnes, J. T. Schofield, G. Wilson, M. Lopez-Valverde, J. L. Hollingsworth, A. F. C. Bridger, and J. Schaeffer (1999), General circulation model simulations of the Mars Pathfinder atmospheric structure investigation/meteorology data, *J. Geophys. Res.*, *104*, 8957–8974.

Hinson, D. P., R. A. Simpson, J. D. Twicken, G. L. Tyler, and F. M. Flasar (1999), Initial results from radio occultation measurements with Mars Global Surveyor, *J. Geophys. Res.*, *104*, 26,997–27,012.

Jacchia, L. G., and J. Slowey (1962), Accurate drag determinations for eight artificial satellites: Atmospheric densities and temperatures, *SAO Spec. Rep. 100*, NASA, Washington, D. C.

Jacobson, R. A., S. P. Synnott, and J. K. Campbell (1989), The orbits of the satellites of Mars from spacecraft and earthbased observations, *Astron. Astrophys.*, *225*, 548–554.

Justus, C. G., and D. L. Johnson (2001), Mars Global Reference Atmospheric Model 2001 version (Mars-GRAM 2001): Users guide, *NASA Tech. Memo., NASA/TM-2001-210961*.

Justus, C. G., B. F. James, S. W. Bougher, A. F. C. Bridger, R. M. Haberle, J. R. Murphy, and S. Engel (2002), Mars-GRAM 2000: A Mars atmospheric model for engineering applications, *Adv. Space Res.*, *29*, 193–202.

Keating, G. M., and S. W. Bougher (1992), Isolation of major Venus thermospheric cooling mechanism and implications for Earth and Mars, *J. Geophys. Res.*, *97*, 4189–4197.

Keating, G. M., et al. (1998), The structure of the upper atmosphere of Mars: In situ accelerometer measurements from Mars Global Surveyor, *Science*, *279*, 1672–1676.

King-Hele, D. (1987), *Satellite Orbits in an Atmosphere: Theory and Applications*, Springer, New York.

Konopliv, A. S., C. F. Yoder, E. M. Standish, D. N. Yuan, and W. L. Sjogren (2006), A Global solution for the Mars static and seasonal gravity, Mars orientation, Phobos and Deimos masses, and Mars ephemeris, *Icarus*, *182*, 23–50.

Krasnopolsky, V. (2002), Mars' upper atmosphere and ionosphere at low, medium, and high solar activities: Implications for evolution of water, *J. Geophys. Res.*, *107*(E12), 5128, doi:10.1029/2001JE001809.

Lemoine, F. G. (1992), The dynamics of orbiting satellites and gravity model development, Ph.D. thesis, Univ. of Colo., Boulder.

Lemoine, F. G. (2003), mgm1041c gravity field solution, http://pds-geosciences.wustl.edu/geodata/mgs-m-rss-5-sdp-v1/mors_1021/sha/, Geosci. Node, Planet. Data Syst., St. Louis, Mo.

Lemoine, F. G., D. E. Smith, D. D. Rowlands, M. T. Zuber, G. A. Neumann, D. S. Chinn, and D. E. Pavlis (2001), An improved solution of the gravity field of Mars (GMM-2B) from Mars Global Surveyor, *J. Geophys. Res.*, *106*, 23,359–23,376.

Lewis, S. R., and P. R. Barker (2005), Atmospheric tides in a Mars general circulation model with data assimilation, *Adv. Space Res.*, *36*, 2162–2168, doi:10.1016/j.asr.2005.05.122.

Lomb, N. R. (1976), Least-squares frequency analysis of unequally spaced data, *Astrophys. Space Sci.*, *39*, 447–462.

Mars Global Surveyor Project (1995), Mission Plan, final version (MGS 542-405), *JPL Doc. D-12088,* Jet Propul. Lab., Pasadena, Calif.

Marshall, J. A., and S. B. Luthcke (1994), Modeling radiation forces acting on TOPEX/Poseidon for precision orbit determination, *J. Spacecr. Rockets*, *31*, 99–105.

Mase, R. A., P. Antreasian, J. L. Bell, T. L. Martin-Mut, and J. C. J. Smith (2005), Mars Odyssey navigation experience, *J. Spacecr. Rockets*, *42*, 386–393.

NASA (2005), Planetary protection provisions for robotic extraterrestrial missions, *Procedural Requirements NPR 8020.12C*, Washington, D. C.

Nier, A. O., and M. B. McElroy (1977), Composition and structure of Mars' upper atmosphere: Results from the neutral mass spectrometers on Viking 1 and 2, *J. Geophys. Res.*, *82*, 4341–4349.

Pace, G. D., et al. (2000), Mars Surveyor 2001 mission plan, revision B Revision B (MSP 722-201), *JPL Doc. D-16303,* Jet Propul. Lab., Pasadena, Calif.

Pavlis, D. E., S. G. Poulose, and J. J. McCarthy (2006), GEODYN operations manuals, report, SGT Inc., Greenbelt, Md.

Smith, D. E., M. T. Zuber, and G. A. Neumann (2001), Seasonal variations of snow depth on Mars, *Science*, *294*, 2141–2146, doi:10.1126/science.1066556.

Smith, D. E., M. T. Zuber, M. T. Torrence, and P. J. Dunn (2003), Estimating the k2 tidal gravity Love number of Mars, *Eos Trans. AGU, Fall Meet. Suppl.*, *84*(46), Abstract P31A-05.

Smith, J. C., and J. L. Bell (2005), 2001 Mars Odyssey aerobraking, *J. Spacecr. Rockets*, *42*, 406–415.

Standish, E. M., X. X. Newhall, J. G. Williams, and W. M. Folkner (1995), JPL planetary and lunar ephemerides, DE403/LE403, *Tech. Rep. JPL IOM 314.10-127*, Jet Propul. Lab., Pasadena, Calif.

Stewart, A. I. F. (1987), Revised time dependent model of the Martian atmosphere for use in orbit lifetime and sustenance studies, *Tech. Rep. JPL PO NQ-802429,* Univ. of Colo., Boulder.

Takashima, N., and R. G. Wilmoth (2002), Aerodynamics of Mars Odyssey, paper presented at Atmospheric Flight Mechanics Conference and Exhibit, Am. Inst. of Aeronaut. and Astronaut., Monterey, Calif.

Tolson, R. H., G. M. Keating, B. E. George, P. E. Escalera, M. R. Werner, A. M. Dwyer, and J. L. Hanna (2005), Application of accelerometer data to Mars Odyssey aerobraking and atmospheric modeling, *J. Spacecr. Rockets*, *42*, 435–443.

Tyler, G. L., G. Balmino, D. P. Hinson, W. L. Sjogren, D. E. Smith, R. Woo, S. W. Asmar, M. J. Connally, C. L. Hamilton, and R. A. Simpson (1992), Radio science investigations with Mars Observer, *J. Geophys. Res.*, *97*, 7759–7779.

Tyler, G. L., G. Balmino, D. P. Hinson, W. L. Sjogren, D. E. Smith, R. A. Simpson, S. W. Asmar, P. Priest, and J. D. Twicken (2001), Radio science observations with Mars Global Surveyor: Orbit insertion through one Mars year in mapping orbit, *J. Geophys. Res.*, *106*, 23,327–23,348.

Wilmoth, R. G., D. F. Rault, F. M. Cheatwood, W. C. Engelund, and R. W. Shane (1999), Rarefied aerothermodynamic predictions for Mars Global Surveyor, *J. Spacecr. Rockets*, *36*, 314–322.

Withers, P. G. (2006), Mars Global Surveyor and Mars Odyssey accelerometer observations of the Martian upper atmosphere during aerobraking, *Geophys. Res. Lett.*, *33*, L02201, doi:10.1029/2005GL024447.

Withers, P., and M. Mendillo (2005), Response of peak electron densities in the Martian ionosphere to day-to-day changes in solar flux due to solar rotation, *Planet. Space Science*, *53*(14-15), 1401–1418.

Withers, P. G., S. W. Bougher, and G. M. Keating (2003), The effects of topographically controlled thermal tides in the Martian upper atmosphere as seen by MGS accelerometer, *Icarus*, *164*, 14–32.

Yoder, C. F., A. S. Konopliv, D. N. Yuan, and E. M. Standish (2003), Fluid core size of Mars from detection of the solar tide, *Science*, *300*, 299–303, doi:10.1126/science.1079645.

F. G. Lemoine and D. E. Smith, Solar System Exploration Division, NASA Goddard Space Flight Center, Code 926, Greenbelt, MD, USA.

E. Mazarico and M. T. Zuber, Department of Earth, Atmospheric and Planetary Sciences, Massachusetts Institute of Technology, 77 Massachusetts Avenue, Cambridge, MA 02139, USA. (mazarico@mit.edu)